

Resonant forward scattered field in high saturation regime: Elastic and inelastic contributions

C. C. Kwong,^{1,2,*} T. Wellens,³ K. Pandey,⁴ and D. Wilkowski^{1,2,5}

¹*Nanyang Quantum Hub, School of Physical and Mathematical Sciences, Nanyang Technological University, 21 Nanyang Link, Singapore 637371, Singapore.*

²*MajuLab, International Joint Research Unit UMI 3654, CNRS, Université Côte d'Azur, Sorbonne Université, National University of Singapore, Nanyang Technological University, Singapore.*

³*Physikalisches Institut, Albert-Ludwigs-Universität, Hermann-Herder-Str. 3, D-79104 Freiburg, Germany.*

⁴*Department of Physics, Indian Institute of Technology Guwahati, Guwahati, Assam 781039, India.*

⁵*Centre for Quantum Technologies, National University of Singapore, 117543 Singapore, Singapore.*

We measure the resonant forward scattering of light by a highly saturated atomic medium through the flashes emitted immediately after an abrupt extinction of the probe beam. Comparing our measurements to a model based on Maxwell-Bloch equations, our experimental results are consistent with contributions from only the elastic component, whereas the attenuation of the coherent transmission power is linked to the elastic and inelastic scatterings. In the large saturation regime and at the vicinity of the atomic resonance, we derive an asymptotic expression relating the elastic scattering power to the forward scattered power.

I. INTRODUCTION

When a quasi-resonant laser beam is shined on an ensemble of atomic emitters, the light undergoes scattering by the randomly positioned atoms. This process depletes photons from the incoming beam, resulting in an attenuation of the power in the coherent transmission. At low intensity, the scattering events are elastic with well-defined phase such that the process remains coherent. Light scattering and transport become more complex at high incident intensity [1], when the atomic transition becomes saturated. Additional inelastic scattering contributions lead to the well-known Mollow triplet [2, 3]. The coherent transport of light through the medium is also altered. For instance, inelastic light scattering reduces the contrast of coherent backscattering [4–7]. Due to the saturation effect, the propagation of light also becomes nonlinear inside the medium. It further leads to the phenomenon of self-induced transparency [8], which provides one method where the optical precursors [9], can be separately measured from the main pulse [10, 11].

In the steady-state regime, energy conservation states that the optical power attenuated in the coherent transmission is converted to the total scattered power, which consists of both elastic and inelastic contributions. In addition, if one considers a beam falling on a slab, the superposition principle, in the far field along the forward direction, leads to $E_t = E_0 + E_s$. Here, the transmitted field E_t is interpreted as a coherent superposition between the incident field E_0 and the forward scattered field E_s , the latter being a coherent field built up on elastic scattering only. This reasoning leads to the remarkable result that the forward scattered field is governed by

elastic events whereas the flux of photons scattered into other directions is linked to the total scattering events, including both elastic and inelastic processes.

A direct measurement of the forward scattered light in the steady-state is hindered by its superposition with the incident field. Fortunately, in the transient regime, the measurement of the steady-state E_s becomes accessible. In particular, the flash effect [12, 13] has been used to experimentally measure the forward scattered field E_s in the linear regime. The coherent emission of a flash is achieved by abruptly switching off the incident probe, so that the atoms in the medium undergo free induction decay (FID) [14–17]. When the medium has a large optical depth, the FID appears as a flash of light during probe extinction, with a time scale shorter than the natural lifetime of the transition [18]. Since the response time of the atoms is finite, E_s remains continuous across any abrupt change to the probe beam. Thus, a detector placed in the exact forward direction will initially measure an optical power P_s that is associated with the field E_s . The phase of E_s , relative to E_0 can be extracted by measuring the incident power P_0 and the steady-state transmitted power P_t [12], or by abrupt phase variation of the incident field [18].

In this article, we analyse the emission of flashes in the saturated regime at large optical depth. We perform experimental measurements of the steady-state transmittance and peak flash power as functions of probe beam detuning and saturation parameter. The peak flash power gives a direct measurement of the forward scattered power. We compare the experimental results with a model based on the Maxwell-Bloch equation, showing that only the elastic component contributes to the forward scattered field. The Maxwell-Bloch equation is commonly used to study the propagation of light through an atomic medium (see a recent work in Ref. [19]). We then discuss at large saturation parameter, how the for-

* changchikwong@ntu.edu.sg

ward scattered power can allow us to determine the elastic scattering power. The paper is organized as follows. In Section II, we derive the Maxwell-Bloch equations using a two-level model, focusing on the calculation of experimentally measured quantities such as the transmitted power and the forward scattered power. The experimental results are presented and compared to the theoretical predictions in Section III. This is followed by a further discussion of the link between the forward scattered power and elastic scattering power in Section IV.

II. THEORETICAL MODEL

In this section, we present our model to describe the coherent transmission of light in the saturated regime. The coherent forward-propagating field inside a two-level atomic cloud can be written as a sum of two fields:

$$E_t(\mathbf{r}, t) = E_0(\mathbf{r}, t) + E_s(\mathbf{r}, t), \quad (1)$$

where $\mathbf{r} = (x, y, z)$, with z directed along the propagation direction. The first term on the right hand side corresponds to the incident laser field:

$$E_0(\mathbf{r}, t) = E_0(x, y)e^{ikz}\Theta(t_{\text{sw}} - t), \quad (2)$$

which is suddenly switched off at time t_{sw} . The wave number of the probe beam is denoted by k . For simplicity, we neglect the finite propagation time of the light through the atomic medium. Θ is the unit step function. The amplitude $E_0(x, y) = E_0 \exp[-(x^2 + y^2)/w_0^2]$ exhibits a Gaussian profile with a beam waist of w_0 . We assume that the Rayleigh length is much larger than the cloud size, so that the waist can be taken to be constant inside the cloud. The maximum amplitude E_0 is related to a saturation parameter $s_0 = 2|\Omega_0|^2/\Gamma^2$, where $\Omega_0 = -E_0d/\hbar$ and $d^2 = 3\pi\epsilon_0\hbar\Gamma/k^3$. Γ is the transition linewidth, d is the reduced electric dipole moment, \hbar is the reduced Planck constant, and ϵ_0 is the vacuum permittivity.

The last term in Eq. (1), $E_s(\mathbf{r}, t)$, denotes the field which is coherently scattered by the atoms in forward direction. The atomic density in our experiments (see Section III A) is low enough to put us in the dilute regime of light scattering, where each atom scatters light independently. Upon neglecting the propagation time, we obtain:

$$E_s(\mathbf{r}, t) = -\frac{3i\pi\hbar\Gamma}{dk^2} \int_{-\infty}^z dz' \rho(\mathbf{r}')e^{ik(z-z')}\sigma_-(\mathbf{r}', t), \quad (3)$$

where $\mathbf{r}' = (x, y, z')$ and

$$\rho(\mathbf{r}) = \rho \exp\left[-\frac{x^2}{2R_{\parallel}^2} - \frac{y^2 + z^2}{2R_{\perp}^2}\right] \quad (4)$$

denotes the density profile of the ellipsoidal cloud. R_{\parallel} (R_{\perp}) is the axial (equatorial) radius of the cloud. $\sigma_-(\mathbf{r}', t)$ refers to the first component of the atomic Bloch vector (see below), which gives rise to coherent scattering of light [3].

A. Bloch equations

With strontium atoms laser-cooled on the narrow intercombination line (see Section III A), the resulting cold atomic cloud still experiences residual Doppler broadening. To take this into account, the component $\sigma_-(\mathbf{r}, t)$ of the atomic Bloch vector is calculated with an average over the atomic velocity distribution $g(v)$:

$$\sigma_-(\mathbf{r}, t) = \int_{-\infty}^{\infty} dv g(v)\sigma_-^{(v)}(\mathbf{r}, t). \quad (5)$$

The velocity distribution is a Gaussian distribution with a standard deviation \bar{v} ,

$$g(v) = \frac{1}{\sqrt{2\pi\bar{v}}} \exp\left(-\frac{v^2}{2\bar{v}^2}\right). \quad (6)$$

For a given velocity v , the atomic Bloch vector fulfills the following optical Bloch equations in the rotating wave approximation:

$$\begin{aligned} \frac{d}{dt}\sigma_-^{(v)}(\mathbf{r}, t) &= \left(i(\delta - kv) - \frac{\Gamma}{2}\right)\sigma_-^{(v)}(\mathbf{r}, t) - i\frac{\Omega_t(\mathbf{r}, t)}{2}\sigma_z^{(v)}(\mathbf{r}, t), \\ \frac{d}{dt}\sigma_+^{(v)}(\mathbf{r}, t) &= \left(-i(\delta - kv) - \frac{\Gamma}{2}\right)\sigma_+^{(v)}(\mathbf{r}, t) + i\frac{\Omega_t^*(\mathbf{r}, t)}{2}\sigma_z^{(v)}(\mathbf{r}, t), \\ \frac{d}{dt}\sigma_z^{(v)}(\mathbf{r}, t) &= -i\Omega_t^*(\mathbf{r}, t)\sigma_-^{(v)}(\mathbf{r}, t) + i\Omega_t(\mathbf{r}, t)\sigma_+^{(v)}(\mathbf{r}, t) - \Gamma\left[\sigma_z^{(v)}(\mathbf{r}, t) + 1\right]. \end{aligned} \quad (7)$$

The local Rabi frequency is denoted by $\Omega_t(\mathbf{r}, t) = -E_t(\mathbf{r}, t)d/\hbar$, where $E_t(\mathbf{r}, t)$ is given by Eqs. (1)–(3). In Eq. (7), we disregard the change of atomic velocities caused by collisions between the atoms (not relevant in

the regime of small density and low temperatures realized in our experiment) and recoils due to scattering of photons (since we are concerned with the forward scattered fields).

The total power of the coherently transmitted light, integrated over the laser beam transverse profile, reads

$$P_t(t) = \frac{c_0 \epsilon_0}{2} \int_{-\infty}^{\infty} dx \int_{-\infty}^{\infty} dy |E_t(x, y, \infty, t)|^2, \quad (8)$$

where c_0 is the speed of light in vacuum. We derive optical powers instead of intensities, since the incident light has a transverse Gaussian profile, and the photodetector effectively integrates over the intensities in this transverse direction. Moreover, the transverse beam profile should be properly taken into account because of the nonlinear response of the atomic medium. We also assume that the light rays propagate parallel to the optical axis, z , disregarding linear and nonlinear focusing or defocusing effect on the beam due to transverse gradients of the medium refractive index. We normalize the transmitted power to the total incident power

$$P_0 = \frac{c_0 \epsilon_0}{2} \int_{-\infty}^{\infty} dx \int_{-\infty}^{\infty} dy |E_0(x, y)|^2 = \frac{\pi c_0 \epsilon_0 w_0^2 |E_0|^2}{4}, \quad (9)$$

and we introduce the on-resonant optical depth up to the point z in the cloud

$$\zeta(\mathbf{r}) = \int_{-\infty}^z \frac{dz'}{\ell_0(\mathbf{r}')} = \frac{6\pi}{k^2} \int_{-\infty}^z dz' \rho(\mathbf{r}'). \quad (10)$$

We stress that the above optical depth is defined in the absence of Doppler broadening. Furthermore, $\ell_0(\mathbf{r}') = 1/[\sigma_0 \rho(\mathbf{r}')]$, denotes the mean free path in a dilute medium of point scatterers. $\sigma_0 = 6\pi/k^2$ is the on-resonance scattering cross section of light. The corre-

sponding resonant optical depth is

$$b_0 = \lim_{z \rightarrow \infty} \zeta(\mathbf{r}). \quad (11)$$

It is considered to be independent of the transverse coordinates, since the beam waist is smaller than the smallest diameter of the atomic cloud ellipsoid (see Section III A). This allows us to approximate the geometry of the medium as a slab. Our problem becomes rotationally invariant around the optical axis (z -axis). The off-center parts of the beam are taken into account by a transverse-dependent saturation parameter,

$$s(x, y) = s_0 \exp \left[-2 \frac{x^2 + y^2}{w_0^2} \right]. \quad (12)$$

Moreover, we introduce dimensionless fields with constant propagation phase as follows

$$\mathcal{E}_t(\zeta, s, t) = \frac{E_t(\mathbf{r}, t)}{E_0(x, y)} e^{-ikz}, \quad (13)$$

$$\mathcal{E}_s(\zeta, s, t) = \frac{E_s(\mathbf{r}, t)}{E_0(x, y)} e^{-ikz}. \quad (14)$$

Similarly, the atomic Bloch vector is rescaled according to:

$$\tilde{\sigma}_{\mp}^{(v)}(\zeta, s, t) = -\frac{\hbar \Gamma \sigma_{\mp}^{(v)}(\mathbf{r}, t)}{dE_0(x, y)} e^{\mp ikz}, \quad (15)$$

$$\tilde{\sigma}_z^{(v)}(\zeta, s, t) = \sigma_z^{(v)}(\mathbf{r}, t) \quad (16)$$

We use the same rescaling for the velocity-averaged quantities, and Eqs. (1-3) become:

$$\mathcal{E}_t(\zeta, s, t) = \Theta(t_{\text{sw}} - t) + \mathcal{E}_s(\zeta, s, t), \quad (17)$$

$$\mathcal{E}_s(\zeta, s, t) = \frac{i}{2} \int_0^{\zeta} d\zeta' \tilde{\sigma}_-(\zeta', s, t). \quad (18)$$

The correspondingly modified Bloch equations are

$$\begin{aligned} \frac{1}{\Gamma} \frac{d}{dt} \tilde{\sigma}_-^{(v)}(\zeta, s, t) &= \left(\frac{i}{\Gamma} (\delta - kv) - \frac{1}{2} \right) \tilde{\sigma}_-^{(v)}(\zeta, s, t) - i \frac{\mathcal{E}_t(\zeta, s, t)}{2} \tilde{\sigma}_z^{(v)}(\zeta, s, t) \\ \frac{1}{\Gamma} \frac{d}{dt} \tilde{\sigma}_+^{(v)}(\zeta, s, t) &= \left(-\frac{i}{\Gamma} (\delta - kv) - \frac{1}{2} \right) \tilde{\sigma}_+^{(v)}(\zeta, s, t) + i \frac{\mathcal{E}_t^*(\zeta, s, t)}{2} \tilde{\sigma}_z^{(v)}(\zeta, s, t) \\ \frac{1}{\Gamma} \frac{d}{dt} \sigma_z^{(v)}(z, s, t) &= -1 - \frac{is}{2} \mathcal{E}_t^*(\zeta, s, t) \tilde{\sigma}_-^{(v)}(\zeta, s, t) + \frac{is}{2} \mathcal{E}_t(\zeta, s, t) \tilde{\sigma}_+^{(v)}(\zeta, s, t) - \tilde{\sigma}_z^{(v)}(\zeta, s, t) \end{aligned} \quad (19)$$

The total coherently transmitted power is obtained by rewriting Eq. (8) in the new variables:

$$\frac{P_t(t)}{P_0} = \int_0^{s_0} \frac{ds}{s_0} |\mathcal{E}_t(b_0, s, t)|^2. \quad (20)$$

If $t_{\text{sw}} \gg 1/\Gamma$, a steady-state regime is achieved before the probe beam is switched off. This regime is obtained by setting the time derivatives in Eq. (19) to zero, thereby

expressing the Bloch vector as an analytical function of the field \mathcal{E}_t . The resulting integral in Eq. (18) can be solved by iteration. Using this solution in Eq. (20) yields the steady-state transmitted power.

Just after switching off the probe beam, the transmitted field jumps from $\mathcal{E}_t = 1 + \mathcal{E}_s$ to $\mathcal{E}_t = \mathcal{E}_s$ [see Eq. (17)]. The corresponding peak power of the flash is therefore

obtained as:

$$\frac{P_s}{P_0} = \int_0^{s_0} \frac{ds}{s_0} |\mathcal{E}_s(b_0, s)|^2, \quad (21)$$

where $\mathcal{E}_s(b_0, s)$ is the steady-state value of forward scattering.

III. EXPERIMENTAL RESULTS

A. Experimental setup and parameters

The experimental setup is sketched in Fig. 1(a). A $\lambda = 689$ nm laser probes the $^1S_0 \rightarrow ^3P_1$ intercombination line transition of a cold ^{88}Sr atomic ensemble, where the natural linewidth is $\Gamma/2\pi = 7.5$ kHz. Cooling and trapping details of the ^{88}Sr atoms are discussed in Ref. [20]. In brief, atoms are laser-cooled in a magneto-optical trap to a final temperature of $T = 3.3$ μK . The experiment is performed 10 ms after the atoms are released from the magneto-optical trap. The cloud takes an ellipsoidal shape with an axial radius of $R_{\parallel} = 240(10)$ μm along the vertical direction, and an equatorial radius of $R_{\perp} = 380(30)$ μm . The cloud consists of of $2.5(5) \times 10^8$ atoms, leading to a peak density of $\rho = 4.6 \times 10^{11}$ cm^{-3} . From the transmission measurement at low intensity, we find that the cloud has an optical depth of $b = 19(3)$. This corresponds to a resonant optical depth at zero temperature of $b_0 = 115(10)$ [13]. The two optical depths are related by $b = b_0 g(k\bar{v}/\Gamma)$, where $g(x) = \sqrt{\pi/8} \exp(1/8x^2) \text{erfc}(1/\sqrt{8}x)/x$. \bar{v} is the thermal velocity of the atoms, defined by $\bar{v} = \sqrt{k_B T/m}$, with k_B Boltzmann factor and m the atomic mass.

Importantly, we note that the cloud is optically dilute ($\rho\lambda^3 = 0.5$). Thus, we can neglect effects coming from sub- and superradiance [21–24]. Modifications of the scattering of light due to density effects [25–32] are also not expected to play a role here.

We apply a 1.4 G magnetic field along the linear polarization direction of the probe beam. This lifts the degeneracy of the excited 3P_1 state, allowing us to probe a two-level system composed of the magnetically insensitive $m_J = 0 \rightarrow m_J = 0$ transition of the intercombination line [see Fig. 1(b)]. The probe beam is focused to a waist of 150 μm , its Rayleigh length is $z_R = \pi w_0^2/\lambda \simeq 10$ cm, thus satisfying the assumptions, $w_0 \ll R_{\parallel}$, R_{\perp} and $z_R \gg R_{\perp}$, made in the previous section. The power of the incident probe beam can be adjusted between 530 pW and 23 μW by applying different neutral density (ND) filters. For the intercombination line where the saturation intensity is $I_s = 3$ $\mu\text{W cm}^{-2}$, the peak saturation parameter s_0 of the Gaussian probe beam ranges from 0.5 to 21700.

The probe beam is switched on at $t = 0$. To limit the effect of radiation pressure force acting on the atoms, the probe is turned off after a time of $t_{\text{sw}} = 40$ μs , long enough for the steady-state transmission to be achieved. Using an acousto-optic modulator (AOM), the falling

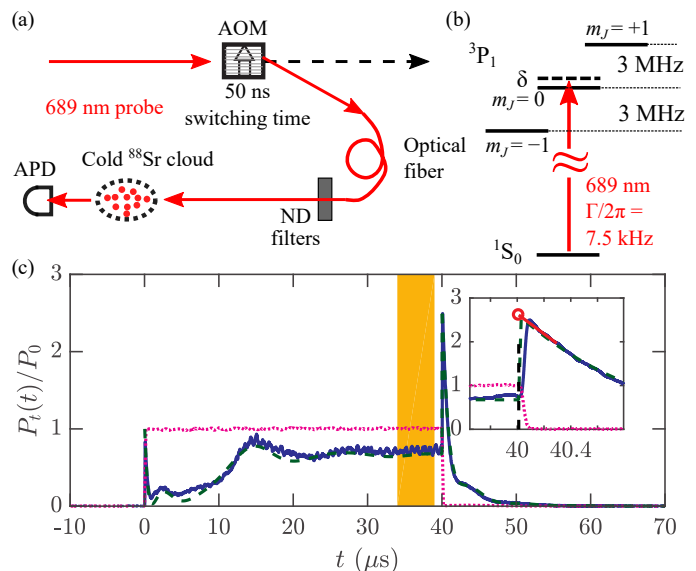


FIG. 1. (a) The experimental setup. (b) The ^{88}Sr intercombination line transition probed in the experiment. The detuning from the $m_J = 0 \rightarrow m_J = 0$ transition is denoted by δ . (c) An example of a temporal signal at $s_0 = 297$ and $\delta = -60$ kHz ($\delta/\Gamma = -8$). The blue solid curve is the experimental data and the green dashed line is a theoretical calculation of the temporal behavior (see Section II). The magenta dotted curve represents the incident probe beam. The orange shaded area indicates the temporal window used to compute the average transmitted power P_t in the steady-state regime. The inset shows the linear extrapolation (red line) in a zoom around the probe extinction. The extrapolated peak value of the flash emission is indicated by the red open circle.

time of the probe beam during the switch-off is 50 ns. This is more than 400 times shorter than the $1/\Gamma = 21$ μs lifetime of the intercombination line. We detect the transmitted light using a 10 MHz bandwidth avalanche photodiode (APD), effectively performing a transverse integral over the transmitted intensity. The measurement signal of the detector is proportional to the transmitted power $P_t(t)$. After the transmission measurement, the atoms are blown away by a strong 461 nm laser tuned on the dipole-allowed $^1S_0 \rightarrow ^1P_1$ transition. The probe beam is then turned on again, with the same duration, to record the incident power P_0 .

The experiment is repeated for different detuning and saturation parameter values of the probe laser. Fig. 1(c) shows an example of the transmission signal $P_t(t)/P_0$ for $s_0 = 297$ and $\delta/\Gamma = -8$, where a superflash (*i.e.* a flash with a normalized amplitude large than 1) is observed after extinction of the probe beam. The green dashed curve is the theoretical curve obtained by solving Eqs. (17,18) together with the Bloch equations (19) using Runge-Kutta integration.

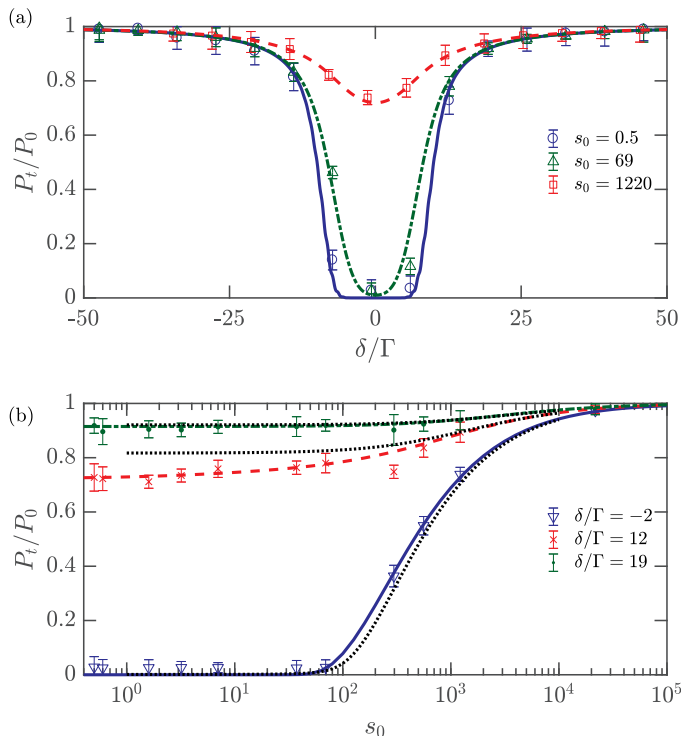


FIG. 2. (a) The steady-state transmitted power as a function of the probe beam detuning, for various saturation parameters. The curves are the theoretical predictions; the blue solid curve is for $s_0 = 0.5$, the green dash-dotted curve is for $s_0 = 69$ and the red dashed curve is for $s_0 = 1220$. (b) The steady-state transmitted power as a function of the probe beam saturation parameter, plotted for three detuning values. The blue solid curve is for the theoretical prediction at $\delta/\Gamma = -2$, the red dashed curve is for the theoretical prediction at $\delta/\Gamma = 12$ and the green dash-dotted curve is for the theoretical prediction at $\delta/\Gamma = 19$. The black dotted lines are the theoretical values of P_t/P_0 , neglecting the Doppler broadening. In (a) and in (b), the data points in the plots are the experimental data for different cases as indicated by the legends. The full range of the error bars represents two standard deviations.

B. Steady-state transmitted power

The experimental value of the steady-state transmitted power P_t is obtained by averaging the transmission signal in a temporal window of $34 \mu\text{s} < t < 39 \mu\text{s}$ [the orange shaded area in Fig. 1(c)].

In Fig. 2(a), we plot the measurements of P_t , at low ($s_0 = 0.5$), intermediate ($s_0 = 69$), and high ($s_0 = 1220$) values of the saturation parameter. In Fig. 2(b), the values of P_t/P_0 are plotted as a function of s_0 , for a probe detuning that is near-resonant ($\delta/\Gamma = -2$), at the low-intensity superflash regime ($\delta/\Gamma = 12$), and at the tail of the absorption window ($\delta/\Gamma = 19$). The curves are the predicted values using Eq. (20), following the procedure outlined just after that equation. The agreement between the theory and the experimental data is excellent.

We observe that up to $s_0 \sim 100$, the values of P_t/P_0 remain similar the low saturation value. As a simple illustration to explain this, we consider the zero temperature case where we find a simple transcendental equation that can be solved numerically for the transmitted saturation parameter, s_t :

$$\left(\frac{4\delta^2}{\Gamma^2} + 1\right) \log\left(\frac{s_t}{s_0}\right) = b_0 \left[\frac{(s_0 - s_t)}{b_0} - 1\right], \quad (22)$$

Integrating the solution over the transverse profile of the Gaussian beam, we find the three dotted lines in Fig. 2(b) for $\delta/\Gamma = -2, 12$ and 19 respectively. We see that this zero temperature case is a good approximation to the Doppler broadened case when either s_t or δ dominates over the Doppler broadening $k\bar{v}/\Gamma$ (see Appendix A for more details). When $s_0 - s_t \ll b_0$, Eq. (22) simplifies to the linear case at low saturation. Therefore, saturation effects start to take place when s_0 is greater than $b_0 = 115$. In this regime, power broadening of the atomic transition dominates over optical depth broadening of the absorption window. The same understanding can be applied to our experiment, even with Doppler broadening. We observe this behavior particularly for the near-resonant case [see blue triangles in Fig. 2(c)]. When $s_0 \leq b_0 \simeq 100$, the steady-state transmission is weak as for the low saturation case. Above $s_0 = 100$, bleaching of the medium occurs, as indicated by the increasing values of P_t as s_0 increases.

The statistical errors are represented by the error bars in Fig. 2. At low saturation, the experimentally measured transmission inside the absorption window is larger than expected. This was already observed in a previous study using the same setup [13]. Since the atomic cloud has a finite size, a small fraction of light can be fully transmitted at the tails of the atomic cloud, and captured by the photodetector. This prevents us to measure a transmittance below 2 %.

C. Peak values of the flash

A flash is emitted in the forward direction, when the probe beam is turned off. The power of the forward transmission just after the extinction of the probe beam is given by the steady-state forward scattered power. In other words, $P_t(t_{\text{sw}}) = P_s$. However, due to the finite response time of the detection scheme, the expected discontinuity in the transmission signal is smoothed out [see inset of Fig. 1(c)]. A linear fit (red line) is applied to extrapolate the peak power of the flash P_s/P_0 , at the time t_{sw} when the laser beam is switched off. Similar procedures were performed in Refs. [12, 13]. The linear fit is performed between $t = t_{\text{sw}} + 50$ ns and $t = t_{\text{sw}} + 200$ ns. In Fig. 3, we plot the peak power of the flash, P_s/P_0 , obtained from the linear extrapolation method. In Fig. 3(a), P_s/P_0 is plotted against δ/Γ for three different saturation parameters $s_0 = 0.5, 69$ and

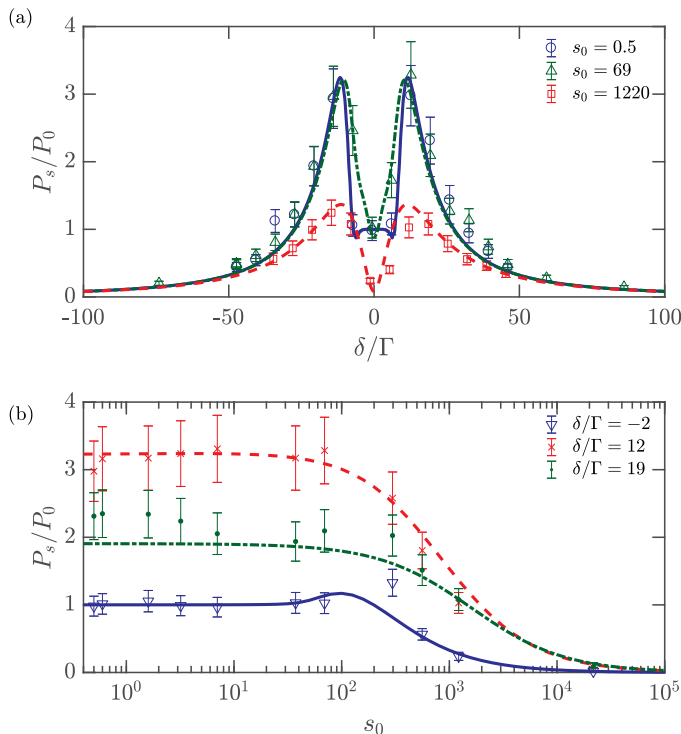


FIG. 3. (a) The peak power of the flash as a function of probe beam detuning, for several saturation parameters of the probe beam. The curves are the theoretical predictions calculated using Eq. (21); the blue solid curve is for $s_0 = 0.5$, the green dash-dotted curve is for $s_0 = 69$ and the red dashed curve is for $s_0 = 1220$. (b) The peak value of the flash as a function of the probe beam saturation parameter, plotted for three detuning values. The blue solid curve is for the theoretical prediction at $\delta/\Gamma = -2$, the red dashed curve is for the theoretical prediction at $\delta/\Gamma = 12$ and the green dash-dotted curve is for the theoretical prediction at $\delta/\Gamma = 19$. In (a) and in (b), the data points in the plots are the experimental data, which, overall, agree very well with the theoretical predictions.

1220. In Fig. 3(b), P_s/P_0 is plotted against s_0 for three different probe detunings, $\delta/\Gamma = -2, 12$ and 19 .

Outside the absorption window, superflashes are emitted when the phase shift of the transmitted field becomes out-of-phase with the incident field. We measure a maximum peak value of the flash at $P_s/P_0 = 3.2$. At even larger detuning values, the atoms interact less with the light, leading to a decrease of the peak value towards zero.

When $s_0 \leq 100$, the transmitted light is strongly absorbed at resonance. This means that the coherently forward scattered field has the same magnitude as the incident field, but with an opposite phase, leading to the observed values of $P_s/P_0 = 1$ [see Fig. 3(a)].

Above $s_0 = 100$, the peak values of the flashes start to decrease for all the three cases plotted in Fig. 3(b). As the atomic transition becomes saturated, the fraction of light that is coherently scattered reduces. This means that

P_s/P_0 also decreases. This is reflected in the reduction of the peak values of the flashes.

In Fig. 3(b), the experimental points at $\delta/\Gamma = 19$ for $s_0 \leq 100$ are systematically higher than the theoretical prediction. Some systematic errors in b_0 or δ could explain these discrepancies, especially when P_s/P_0 vary rapidly either with respect to s_0 or δ/Γ . This could also explain the discrepancy at $s_0 \approx 300$ for the case of $\delta/\Gamma = -2$.

Finally, we note that our approach neglects backaction of the scattered fields, elastic and inelastic, onto the forward-propagating field due to the nonlinear response of the atomic medium [1]. The generally well agreement between the experimental results and the prediction of the model justifies this approximation. The backaction could be important in some cases, such as in parts of a medium not directly illuminated, in optically thick medium where radiation trapping could happen, or at the weak intensity tail of a Gaussian beam where the saturation parameter could be strongly affected by the scattered light.

IV. DISCUSSION

As discussed in section II, the forward scattered field is coherent, so it is built up upon elastic events, even in the strong saturation regime where scattering is mainly inelastic. We now want to improve our intuitive understanding gained from the comparison between experiment and numerical simulations presented in section III by deriving a simple analytical relation linking the forward scattered power to the elastic scattered power. In general, the existence of such a relation is still an open question. However, in the large saturation regime, a simple linear relation between the forward scattered power P_s and the elastic scattered power P_{el} can be found. In this section, we derive this formula and apply it to our experimental data.

At first, we remind that, by the conservation of energy fluxes in the steady-state regime, the total power scattered by the atomic medium is $P_{sca} = P_0 - P_t$. $P_{sca} = P_{el} + P_{in}$ contains both the elastic P_{el} and inelastic P_{in} contributions [3]. Therefore, the transmitted power is simply related to the total scattered power.

Now, to find a relation between P_s and P_{el} , we first consider the resonant case $\delta = 0$, and we take the probe beam to be transversally homogeneous with an area A and an incident saturation parameter of s_0 . We consider also an atomic medium at zero temperature with uniform slab geometry. Finally, we consider the weak absorption limit ($s_t \approx s_0$), which holds for a medium with $b_0 \ll 1$, or for a highly saturated medium with large optical depth. Eq. (22) gives

$$P_t \approx P_0 \left(1 - b_0 \frac{1}{1 + s_0} \right) = P_0 - P_{sca}, \quad (23)$$

where $P_0 = AI_{sat}s_0$. Moreover, we know that the elastic

contribution reads [3]

$$\frac{P_{\text{el}}}{P_0} = \frac{b_0}{(1 + s_0)^2}, \quad (24)$$

and the inelastic scattering contribution reads

$$\frac{P_{\text{in}}}{P_0} = \frac{b_0 s_0}{(1 + s_0)^2}. \quad (25)$$

From Eq. (1), we further have the following relation between P_t , P_0 and P_s .

$$P_t = P_0 + P_s + 2\sqrt{P_0 P_s} \cos \varphi, \quad (26)$$

where φ is the phase difference between E_s and E_0 . In cases where the forward scattered power is weak, i.e., $P_s \ll (P_0 - P_t)$, we can approximate the above equation as:

$$P_t \approx P_0 + 2\sqrt{P_0 P_s} \cos \varphi. \quad (27)$$

At $\delta = 0$, $\varphi = \pi$ regardless of the value of s_0 . Thus, we have

$$\frac{P_s}{P_0} \approx \frac{1}{4} \left(\frac{P_0 - P_t}{P_0} \right)^2. \quad (28)$$

At resonance, when $s_t \approx s_0$, we have $P_s \ll P_0 - P_t$, which justifies our approximation. Using Eqs. (23) and (24), we find that the forward scattered power is proportional to the elastic scattering,

$$\frac{P_s}{P_0} \approx \frac{b_0^2}{4(1 + s_0)^2} = \frac{b_0}{4} \frac{P_{\text{el}}}{P_0}. \quad (29)$$

We further generalize Eq. (29), including Doppler broadening and small detuning, so the linear relation between P_s and P_{el} reads (see details in Appendix B)

$$\frac{P_s}{P_0} \approx \frac{b_0}{4 \cos^2 \varphi} \frac{1}{1 + 4(k\bar{v}/\Gamma)^2 + 4(\delta/\Gamma)^2} \frac{P_{\text{el}}}{P_0}. \quad (30)$$

This final relation is derived for weak attenuation $s_t \approx s_0$, weak forward scattering $P_s \ll P_0 - P_t$ and strong saturation where

$$s_0 \gg 1 + 8(k\bar{v}/\Gamma)^2 + 4(\delta/\Gamma)^2. \quad (31)$$

The above assumptions allow us to rewrite the condition $s_t \approx s_0$ as

$$s_0 \gg b_0. \quad (32)$$

Since we have $b_0 \gg 1$ in this study, $P_s \ll P_0 - P_t$ can also be rewritten as (see Appendix B)

$$s_0 \gg b_0(\delta/\Gamma)^2. \quad (33)$$

Within the framework of the model discussed in Section II, we can also compute directly the total elastic scattering power. Considering only single scattering events,

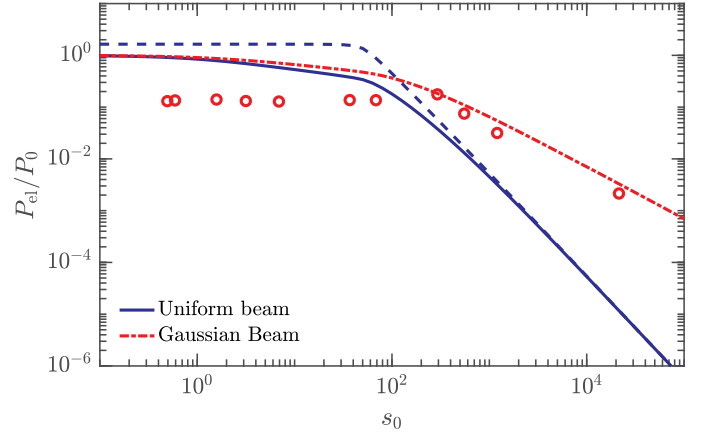


FIG. 4. Plot showing the numerically simulated elastic scattering power and the values obtained from the experimentally accessible quantity P_s using Eq. (30). The curves are simulated results for uniform (blue solid) and Gaussian (red dash-dotted) probe beams, with the details of the simulation provided in the text. The blue dashed line shows the values obtained using Eq. (30) and the numerically simulated values of P_s/P_0 . The red open circles are the extracted elastic scattering power using the experimental results at $\delta/\Gamma = -2$.

we sum up the velocity-averaged elastic scattering power over all the atoms at different positions in the medium

$$\frac{P_{\text{el}}}{P_0} = \int_0^{s_0} \frac{ds}{s_0} \int_0^{b_0} d\zeta \int_{-\infty}^{\infty} dv \frac{g(v) [4(\delta - kv)^2/\Gamma^2 + 1]}{[4(\delta - kv)^2/\Gamma^2 + 1 + \eta]^2}. \quad (34)$$

Here, the steady-state local saturation parameter at a position parametrized by (ζ, s) is given by

$$\eta(\zeta, s) = s |\mathcal{E}_t(\zeta, s)|^2. \quad (35)$$

\mathcal{E}_t with parameter t dropped denotes its steady-state value.

We check the validity of Eq. (30) using Eqs. (21) and (34) to compute P_s and P_{el} , respectively. In Fig. 4, the value of P_{el}/P_0 , directly calculated from the numerical simulation according to Eq. (34), is plotted as the solid blue curve, while the numerically calculated P_s/P_0 is used in Eq. (30) to compute the blue dashed curve. Here, $\delta/\Gamma = 0$, $b_0 = 115$ and $k\bar{v}/\Gamma = 3.4$, thus the two curves converge when $s_0 > b_0$. For $|\delta| > \Gamma$, the convergence is found for $s_0 > b_0(\delta/\Gamma)^2$, according to Eq. (33).

We now aim to extract the elastic scattering power from our transmission measurements. An important difference lies in the Gaussian profile of the probe beam, which requires a transverse integration of the formula Eq. (30). The factor $\cos^2 \varphi$, however, complicates the transverse integration. Fortunately, the value of $\cos \varphi$ saturates to the following at large s_0 (see Appendix B):

$$\cos \varphi \approx -\frac{1}{\sqrt{4(\delta/\Gamma)^2 + 1}}. \quad (36)$$

This suggests that Eq. (30) can be used as an approximation for a Gaussian probe beam, by taking $\cos \varphi$ to be the

value in Eq. (36). Using this approach, we plot the experimental results at $\delta/\Gamma = -2$ (red open circles) in Fig. 4. For $s_0 > b_0(\delta/\Gamma)^2 \simeq 460$, a good agreement is achieved between the experimental results and the red dash-dotted curve calculated numerically according to Eq. (34). The remaining discrepancy may originate from the tails of the Gaussian beam where the saturation parameter is low, and our assumptions do not hold.

At large s_0 , P_{el}/P_0 for the uniform beam case scales as s_0^{-2} , as expected from Eq. (24). For the Gaussian beam case, the numerical results of P_{el}/P_0 scales as s_0^{-1} . The difference between the uniform and Gaussian beam can be understood from the fact that transverse integration is essentially an integration over the saturation parameter (see Eq. (34)). Thus, upon transverse integration, the scaling behavior at large s_0 changes from s_0^{-2} to s_0^{-1} . The experimental estimation of the elastic scattering scales as $s_0^{-0.96(19)}$ for $s_0 > 500$, in agreement with the expected behavior.

V. CONCLUSION

We have performed experimental studies of the forward scattered power in the saturated regime. This quantity is extracted from the peak power of the flash, obtained after abruptly switching off the incident laser beam. Our experimental results are well explained by a model based on Maxwell-Bloch equations, consistent with the fact that only coherent elastic scattering contributes to the forward scattered light. At large saturation and at the vicinity of the resonance, we derived a relation to compute the total power scattered elastically by the atomic medium from the measurement of the forward scattered power. While our relation is valid for a limited range of parameters, it can be readily applied to hot or cold atomic ensembles. Since the total scattered power is also known from the steady state transmission measurement, this allows us to measure the relative contributions of elastic and inelastic scattering. This bears the merit of requiring only a simpler transmission measurement in the transient regime, avoiding more sophisticated measurements of the fluorescence spectrum (see a recent measurement in Ref. [33]).

Finally, several recent works in the linear scattering regime have revealed density-induced cooperative shift and linewidth broadening of optical transitions [19, 25, 29–32]. However, to the best of our knowledge transient coherent phenomena in dense regime have not yet been explored. In particular, in high-saturated regime, the flash effect could be a simple tool to extract elastic scattering, where strong cooperativity is likely to reinforce

it.

ACKNOWLEDGMENTS

The authors thank T. Yang for technical assistance in performing the experiment and data taking, and A. Buchleitner for careful reading of the manuscript. This work was supported by the CQT/MoE funding Grant No. R-710-002-016-271.

Appendix A: The zero temperature approximation

Under thermal averaging, the scattering cross section of an atom in the saturated regime with a local value of saturation parameter η , reads

$$\sigma_{\bar{v}} = \frac{\sigma_0}{1 + \eta} \text{Re} \{G_{\bar{v}}(\delta, \eta)\}, \quad (\text{A1})$$

with

$$G_{\bar{v}}(\delta, \eta) = \sqrt{\frac{\pi}{8}} \frac{\Gamma \sqrt{1 + \eta}}{k\bar{v}} w \left(\frac{\delta + i\Gamma \sqrt{1 + \eta}/2}{\sqrt{2}k\bar{v}} \right), \quad (\text{A2})$$

and $w(z)$ is the Faddeeva function [34]. Here, $\text{Im}\{z\} > 0$, so the Faddeeva function has the following asymptotic expansion [35]:

$$w(z) \approx \frac{i}{\sqrt{\pi}} \left[\frac{1}{z} + \frac{1}{2z^3} + \frac{3}{4z^5} \right]. \quad (\text{A3})$$

For $|\delta + i\Gamma \sqrt{1 + \eta}/2| \gg \sqrt{2}k\bar{v}$, the above asymptotic expansion can be applied throughout the atomic medium. Keeping only the leading term leads us back to the scattering cross section in absence of Doppler broadening, i.e.,

$$\sigma_{\bar{v}} \sim \sigma_0 \frac{\Gamma^2/4}{\delta^2 + \Gamma^2(1 + \eta)/4}, \quad (\text{A4})$$

Thus, for sufficiently large η or δ values, the zero temperature limit is a good approximation. We remind that if η is large, then $\eta \approx s_0 \approx s_t$.

Appendix B: Derivation of Eq. (30)

For a uniform probe beam, with $s_t \approx s_0$, Eq. (34) simplifies to

$$\frac{P_{\text{el}}}{P_0} \approx b_0 \int_{-\infty}^{\infty} dv \frac{g(v) [4(\delta - kv)^2/\Gamma^2 + 1]}{[4(\delta - kv)^2/\Gamma^2 + 1 + s_0]^2}. \quad (\text{B1})$$

After velocity averaging, we find

$$\frac{P_{el}}{P_0} \approx b_0 \left\{ \frac{2 + s_0}{2(1 + s_0)^2} \text{Re} \{G_{\bar{v}}(\delta, s_0)\} - \frac{s_0}{8(1 + s_0)} \left(\frac{\Gamma}{k\bar{v}}\right)^2 [1 - \text{Re} \{G_{\bar{v}}(\delta, s_0)\}] + \frac{s_0}{4(1 + s_0)^{3/2}} \frac{\Gamma\delta}{(k\bar{v})^2} \text{Im} \{G_{\bar{v}}(\delta, s_0)\} \right\} \quad (\text{B2})$$

A further simplification is possible by considering $s_0 \gg 8(k\bar{v}/\Gamma)^2$ so that Eq. (A3) can be applied. Considering further that $s_0 \gg 1 + 4(\delta/\Gamma)^2$, we get

$$\frac{P_{el}}{P_0} \approx \frac{b_0}{s_0^2} \left[1 + 4 \left(\frac{k\bar{v}}{\Gamma}\right)^2 + 4 \left(\frac{\delta}{\Gamma}\right)^2 \right]. \quad (\text{B3})$$

From Eq. (27), under the further constrain of weak forward scattered power $P_s \ll P_0 - P_t$, we find

$$\frac{P_s}{P_0} \approx \frac{(1 - P_t/P_0)^2}{4 \cos^2 \varphi}, \quad (\text{B4})$$

whereas the total scattered power is given by

$$\begin{aligned} \frac{P_0 - P_t}{P_0} &\approx b_0 \int_{-\infty}^{\infty} dv \frac{g(v)}{[4(\delta - kv)^2/\Gamma^2 + 1 + s_0]^2} \\ &= \frac{b_0}{1 + s_0} \text{Re} \{G_{\bar{v}}(\delta, s_0)\} \approx \frac{b_0}{s_0}. \end{aligned} \quad (\text{B5})$$

Upon substituting the above relation into Eq. (B4), we get

$$\frac{P_s}{P_0} \approx \frac{b_0^2}{4s_0^2 \cos^2 \varphi}. \quad (\text{B6})$$

Inserting Eq. (B3) in the above equation leads to Eq. (30).

We further discuss the range of δ/Γ for Eq. (B4) to be valid. In this large saturation regime of $s_0 \gg 8(k\bar{v}/\Gamma)^2$, we can ignore Doppler broadening. We then approximate the effective optical depth \mathcal{B} and the phase shift of the

transmitted field ϕ as

$$\begin{aligned} \mathcal{B} &\approx \frac{b_0}{4(\delta/\Gamma)^2 + 1 + s_0}, \\ \phi &\approx -\frac{b_0(\delta/\Gamma)}{4(\delta/\Gamma)^2 + 1 + s_0} \end{aligned} \quad (\text{B7})$$

The forward scattered field, relative to the incident field at the output surface of the medium, is $E_s/E_0 = \exp(-\mathcal{B} + i\phi) - 1$. Thus, the forward scattered power is given by

$$\frac{P_s}{P_0} = 1 + \exp(-\mathcal{B}) - 2 \exp(-\mathcal{B}/2) \cos \phi. \quad (\text{B8})$$

The total scattered power is given by

$$\frac{P_0 - P_t}{P_0} = 1 - \exp(-\mathcal{B}). \quad (\text{B9})$$

Thus, the inequality $P_s < P_0 - P_t$ leads to

$$\exp(-\mathcal{B}/2) < \cos \phi. \quad (\text{B10})$$

if we further have $s_0 \gg 1 + 4(\delta/\Gamma)^2$, b_0 , then \mathcal{B} , $\phi \ll 1$ and we find that the above inequality becomes

$$\phi^2 < \mathcal{B}. \quad (\text{B11})$$

In our case where $b_0 \gg 1$, we find the following condition for Eq. (B4) to be valid, i.e.,

$$s_0 \gg b_0 \left(\frac{\delta}{\Gamma}\right)^2. \quad (\text{B12})$$

We further note that in the regime of large saturation that we are considering, the forward scattered field can be approximated as

$$\frac{E_s}{E_0} \approx -\frac{\mathcal{B}}{2} + i\phi, \quad (\text{B13})$$

from which we find $\cos \varphi$ to saturate to the following value at large s_0 ,

$$\cos \varphi \approx -\frac{1}{\sqrt{4(\delta/\Gamma)^2 + 1}}. \quad (\text{B14})$$

-
- [1] T. Binniger, V. N. Shatokhin, A. Buchleitner, and T. Wellens, "Nonlinear quantum transport of light in a cold atomic cloud," *Phys. Rev. A* **100**, 033816 (2019).
 [2] B. R. Mollow, "Power spectrum of light scattered by two-

- level systems," *Phys. Rev.* **188**, 1969–1975 (1969).
 [3] C. Cohen-Tannoudji, J. Dupont-Roc, and G. Grynberg, *Atom-Photon Interactions: Basic Processes and Applications* (Wiley-VCH, New York, 2004).

- [4] D. Wilkowski, Y. Bidel, T. Chanelière, D. Delande, T. Jonckheere, B. Klappauf, G. Labeyrie, C. Miniatura, C. A. Müller, O. Sigwarth, and R. Kaiser, “Coherent backscattering of light by resonant atomic dipole transitions,” *J. Opt. Soc. Am. B* **21**, 183–190 (2004).
- [5] T. Chanelière, D. Wilkowski, Y. Bidel, R. Kaiser, and C. Miniatura, “Saturation-induced coherence loss in coherent backscattering of light,” *Phys. Rev. E* **70**, 036602 (2004).
- [6] T. Wellens, B. Grémaud, D. Delande, and C. Miniatura, “Coherent backscattering of light by two atoms in the saturated regime,” *Phys. Rev. A* **70**, 023817 (2004).
- [7] S. Balik, P. Kulatunga, C. I. Sukenik, M. D. Havey, D. V. Kupriyanov, and I. M. Sokolov, “Strong-field coherent backscattering of light in ultracold atomic ^{85}Rb ,” *J. Mod. Opt.* **52**, 2269–2278 (2005).
- [8] S. L. McCall and E. L. Hahn, “Self-induced transparency,” *Phys. Rev.* **183**, 457–485 (1969).
- [9] For a pulse travelling through a dispersive medium, the optical precursor is the front of the pulse which travels at the vacuum speed of light [36, 37]. It has been observed in solid state [38] and cold atomic systems [39, 40].
- [10] B. Macke and B. Ségard, “Optical precursors with self-induced transparency,” *Phys. Rev. A* **81**, 015803 (2010).
- [11] R. Marskar and U. L. Österberg, “Linear and nonlinear optical precursors in inhomogeneously broadened two-level media,” *Phys. Rev. A* **86**, 063826 (2012).
- [12] M. Chalony, R. Pierrat, D. Delande, and D. Wilkowski, “Coherent flash of light emitted by a cold atomic cloud,” *Phys. Rev. A* **84**, 011401(R) (2011).
- [13] C. C. Kwong, T. Yang, M. S. Pramod, K. Pandey, D. Delande, R. Pierrat, and D. Wilkowski, “Cooperative emission of a coherent superflash of light,” *Phys. Rev. Lett.* **113**, 223601 (2014).
- [14] E. L. Hahn, “Nuclear induction due to free Larmor precession,” *Phys. Rev.* **77**, 297–298 (1950).
- [15] R. G. Brewer and R. L. Shoemaker, “Optical free induction decay,” *Phys. Rev. A* **6**, 2001–2007 (1972).
- [16] K. Toyoda, Y. Takahashi, K. Ishikawa, and T. Yabuzaki, “Optical free-induction decay of laser-cooled ^{85}Rb ,” *Phys. Rev. A* **56**, 1564–1568 (1997).
- [17] U. Shim, S. Cahn, A. Kumarakrishnan, T. Sleator, and J.-T. Kim, “Optical free induction decay in cold ^{85}Rb atoms,” *Jpn. J. Appl. Phys.* **41**, 3688–3692 (2002).
- [18] C. C. Kwong, T. Yang, D. Delande, R. Pierrat, and D. Wilkowski, “Cooperative emission of a pulse train in an optically thick scattering medium,” *Phys. Rev. Lett.* **115**, 223601 (2015).
- [19] S. Jennewein, L. Brossard, Y. R. P. Sortais, A. Browaeys, P. Cheinet, J. Robert, and P. Pillet, “Coherent scattering of near-resonant light by a dense, microscopic cloud of cold two-level atoms: Experiment versus theory,” *Phys. Rev. A* **97**, 053816 (2018).
- [20] T. Yang, K. Pandey, M. S. Pramod, F. Leroux, C. C. Kwong, E. Hajiyev, Z. Y. Chia, B. Fang, and D. Wilkowski, “A high flux source of cold strontium atoms,” *Eur. Phys. J. D* **69**, 226 (2015).
- [21] R. H. Dicke, “Coherence in spontaneous radiation processes,” *Phys. Rev.* **93**, 99–110 (1954).
- [22] M. Gross and S. Haroche, “Superradiance: An essay on the theory of collective spontaneous emission,” *Phys. Rep.* **93**, 301 – 396 (1982).
- [23] S. J. Roof, K. J. Kemp, M. D. Havey, and I. M. Sokolov, “Observation of single-photon superradiance and the cooperative Lamb shift in an extended sample of cold atoms,” *Phys. Rev. Lett.* **117**, 073003 (2016).
- [24] W. Guerin, M. O. Araújo, and R. Kaiser, “Subradiance in a large cloud of cold atoms,” *Phys. Rev. Lett.* **116**, 083601 (2016).
- [25] J. Keaveney, A. Sargsyan, U. Krohn, I. G. Hughes, D. Sarkisyan, and C. S. Adams, “Cooperative Lamb shift in an atomic vapor layer of nanometer thickness,” *Phys. Rev. Lett.* **108**, 173601 (2012).
- [26] S. Balik, A. L. Win, M. D. Havey, I. M. Sokolov, and D. V. Kupriyanov, “Near-resonance light scattering from a high-density ultracold atomic ^{87}Rb gas,” *Phys. Rev. A* **87**, 053817 (2013).
- [27] J. Pellegrino, R. Bourgain, S. Jennewein, Y. R. P. Sortais, A. Browaeys, S. D. Jenkins, and J. Ruostekoski, “Observation of suppression of light scattering induced by dipole-dipole interactions in a cold-atom ensemble,” *Phys. Rev. Lett.* **113**, 133602 (2014).
- [28] J. Javanainen, J. Ruostekoski, Y. Li, and S.-M. Yoo, “Shifts of a resonance line in a dense atomic sample,” *Phys. Rev. Lett.* **112**, 113603 (2014).
- [29] S. Jennewein, M. Besbes, N. J. Schilder, S. D. Jenkins, C. Sauvan, J. Ruostekoski, J.-J. Greffet, Y. R. P. Sortais, and A. Browaeys, “Coherent scattering of near-resonant light by a dense microscopic cold atomic cloud,” *Phys. Rev. Lett.* **116**, 233601 (2016).
- [30] S. L. Bromley, B. Zhu, M. Bishof, X. Zhang, T. Bothwell, J. Schachenmayer, T. L. Nicholson, R. Kaiser, S. F. Yelin, M. D. Lukin, A. M. Rey, and J. Ye, “Collective atomic scattering and motional effects in a dense coherent medium,” *Nat. Commun.* **7**, 11039 (2016).
- [31] L. Corman, J. L. Ville, R. Saint-Jalm, M. Aidelburger, T. Bienaimé, S. Nascimbène, J. Dalibard, and J. Beugnon, “Transmission of near-resonant light through a dense slab of cold atoms,” *Phys. Rev. A* **96**, 053629 (2017).
- [32] C. C. Kwong, D. Wilkowski, D. Delande, and R. Pierrat, “Coherent light propagation through cold atomic clouds beyond the independent scattering approximation,” *Phys. Rev. A* **99**, 043806 (2019).
- [33] L. Ortiz-Gutiérrez, R. C. Teixeira, A. Eloy, D. F. da Silva, R. Kaiser, R. Bachelard, and M. Fouché, “Mollow triplet in cold atoms,” *New J. Phys.* **21**, 093019 (2019).
- [34] M. Abramowitz and I. A. Stegun, *Handbook of Mathematical Functions, With Formulas, Graphs, and Mathematical Tables*, (Dover Publications, Inc., New York, 1974).
- [35] W. Gautschi, “Efficient computation of the complex error function,” *SIAM J. Numer. Anal.* **7**, 187–198 (1970).
- [36] A. Sommerfeld, “Über die Fortpflanzung des Lichtes in dispergierenden Medien,” *Ann. Phys.* **349**, 177–202 (1914).
- [37] L. Brillouin, “Über die Fortpflanzung des Lichtes in dispergierenden Medien,” *Ann. Phys.* **349**, 203–240 (1914).
- [38] J. Aaviksoo, J. Kuhl, and K. Ploog, “Observation of optical precursors at pulse propagation in GaAs,” *Phys. Rev. A* **44**, R5353–R5356 (1991).
- [39] H. Jeong, A. M. C. Dawes, and D. J. Gauthier, “Direct observation of optical precursors in a region of anomalous dispersion,” *Phys. Rev. Lett.* **96**, 143901 (2006).
- [40] D. Wei, J. F. Chen, M. M. T. Loy, G. K. L. Wong, and S. Du, “Optical precursors with electromagnetically induced transparency in cold atoms,” *Phys. Rev. Lett.* **103**, 093602 (2009).